Submission to Atmospheric Measurement Techniques

Near Global Distributions of Overshooting Tops Derived from Terra and Aqua MODIS Observations

Yulan Hong, Stephen W. Nesbitt, Robert J. Trapp, and Larry Di Girolamo

Department of Atmospheric Sciences, University of Illinois Urbana-Champaign, Urbana, Illinois, USA

Corresponding author: Yulan Hong

Email: yulanh@illinois.edu

Abstract

Overshooting cloud tops (OT) form in deep convective storms when strong updrafts overshoot the tropopause. An OT is a well-known indicator for convective updrafts and severe weather conditions. Here, we develop an OT detection algorithm using thermal IR channels and apply this algorithm to about 20-year MODIS data from both Terra and Aqua satellites to form an extensive, near global climatology of OT occurrences. The algorithm is based on a logistic model which is trained using A-Train observations. We demonstrate that the overall accuracy of our approach is about 0.9 when the probability of the OT candidates is larger than 0.9. The OT climatology reveals a pattern that follows the climatology of deep convection, as well as shallow convection over the mid-latitude oceans during winter cold air outbreaks. OTs appear most frequently over the Intertropical Convergence Zone (ITCZ), central and southeast North America, tropical and subtropical South America, southeast and south Asia, tropical and subtropical Africa, and northern middle-high latitudes. OT spatial distributions show strong seasonal and diurnal variabilities. Seasonal OT variations shift with large-scale climate systems such as the ITCZ and local monsoonal systems, including the South Asian Monsoon, North American Monsoon and West African Monsoon, etc. OT diurnal variations agree with the known diurnal cycle of convection: Maximum OT occurrences are in the afternoon over most land area and around midnight over ocean; and the OT diurnal cycle is stronger and more varied over land than over ocean. OTs over land are usually colder than over ocean except around 10:30 am. The top 10 coldest OTs from both Terra and Aqua mostly occur over land and at night. This study provides OT climatology for the first time derived from two-decade MODIS data that represents the longest and stable satellite records.

1. Introduction

An overshooting cloud top (OT) forms when a convective-storm updraft penetrates the level of neutral buoyancy and thus extends into the upper troposphere-lower stratosphere (UTLS). OTs and their associated strong updrafts have been found to be an important transport mechanism for water vapor and other atmospheric constituents into the stratosphere, thus impacting the chemical composition and radiation budget of the UTLS (e.g. Gettelman et al., 2002, 2004). They are often used as indicators of hazardous weather conditions such as strong winds, large hail, flooding, and tornadoes at the Earth's surface (Bedka et al., 2018; Dworak et al., 2012; Marion et al., 2019). More generally, the characteristics of OTs express information about the characteristics of the related updrafts well below cloud top, including the convective mass flux through the troposphere, which is an important parameterized quantity used in global climate models.

In addition to the expectation of a connection between updraft strength and OT depth (Heymsfield et al., 2010), Trapp et al. (2017) has shown a strong link between updraft core area and OT area (OTA), indicating that a relatively intense and wide mid-tropospheric updraft core area will tend to have a large OTA. Given that the direct measurements of updrafts within intense convective environments are either from a few ground-based radars or several field campaigns, these studies suggest a pathway for characterizing global updraft and updraft-size distributions by quantifying the global OT distributions and characteristics from space.

Toward this end, the first step is to detect OTs. Geostationary satellite imagery provides the opportunity to study OT occurrence over a wide region with fine spatial and temporal resolutions. A series of OT detection algorithms have been developed based on geostationary satellite observations. A commonly used OT detection method utilizes the brightness temperature (T_b) difference (BTD) between Infrared (IR) water vapor (WV) and IR window channels (IRW) (Schmetz et al., 1997). The WV-IRW BTD method is based on the fact that water vapor transported into the lower stratosphere absorbs and emits more radiation at a water vapor channel (such as 6.7μm) compared to a window channel (such as 11 μm). Thus, positive BTD is usually observed in the OT regions. However, in convective anvils (e.g. Hong & Di Girolamo, 2020; Setvák et al., 2013) or in polar winter conditions when strong radiation inversions exist near the surface (Ackerman, 1996), positive BTDs are also observed, which pose challenges to differentiate OTs from these cases.

Another commonly used OT detection method is the IR Window (IRW) texture approach (Bedka et al., 2010). This method uses a threshold of 215 K T_b at IR window channel to first select OT candidates. These candidates are also colder than the tropopause temperatures. In the second step, surrounding anvil is sampled at a ~ 8 km radius in 16 directions. At each direction, pixels with T_{b11} colder than 225 K are included in calculating cirrus mean T_{b11}. The selected candidate is considered as an OT if the T_{b11} difference between the pixel and its surrounding cirrus is larger than a threshold of 6.5 K. The IRW texture approach has been widely applied for OT detections observed from space such as geostationary satellite imagery and Moderate Resolution Imaging Spectroradiometer (MODIS) (Bedka, 2011; Dworak et al., 2012; Griffin, 2017; Griffin et al., 2016; Monette et al., 2012; Proud, 2015). However, the strictly fixed thresholds of IRW texture method limit its ability to detect warm OTs that commonly occur in the mid-latitude regions, leading to seasonal and regional biases (Bedka & Khlopenkov, 2016). Based on the visible (VIS) and IR imagery, Bedka and Khlopenkov (2016) developed a new

83 probabilistic OT detection algorithm to minimize the dependence of IRW texture method on
84 thresholds. Khlopenkov et al. (2021) further updated this algorithm by incorporating the
85 normalized tropopause temperature, surrounding anvil area and spatial uniformity. Improved
86 accuracy is achieved with this probabilistic OT detection algorithm compared to the IRW texture
87 method.

88   Observations from spaceborne active sensors have also been used for exploring OT
89 detections. For instance, the cloud profiling radar (CPR) on CloudSat (Stephens et al., 2008) was
90 used for validating the passive satellite-based OT detection methods (Bedka et al., 2010; Dworak
91 et al., 2012; Rysman et al., 2017), calculating the heights of OTs (Griffin et al., 2016), and
92 understanding WV-IRW BTD variability in OT regions (Setvák et al., 2013). The combined
93 CloudSat-CALIPSO (Cloud-Aerosol Lidar and Infrared Pathfinder Satellite Observation) data
94 was also used for detecting OTs, which led to the creation of a 12-year OT database (Li et al.,
95 2022). As demonstrated by these studies, the CloudSat-CALIPSO observations are powerful in
96 detecting OTs and gauging OT depths, but they are only available in a narrow swath that leads to
97 a lack of knowledge of three-dimensional (3-D) OT structures and large uncertainties in their
98 coverage (Astin et al., 2001). The precipitation radar on Tropical Rainfall Measuring Mission
99 (TRMM) or Global Precipitation Mission (GPM) can provide 3-D depictions of storm structures.
100 The precipitation radar observations have been used to investigate OT climatology including
101 their geodistributions, area and diurnal cycles in the tropical regions ($20°S – 20°$N) (Alcala &
102 Dessler, 2002; Liu & Zipser, 2005) and over broader areas ($60°S – 60°$N) (Hourngir et al., 2021;
103 Liu et al., 2020; Liu & Liu, 2016).

104   In addition, using three water vapor channels of the Advanced Microwave Sounding Unit
105 B (AMSU-B), convective overshooting detection method was developed through the microwave
106 technique (Hong et al., 2005). A seven-year OT climatology based on AMSU-B was derived in
107 the tropical and subtropical areas that shows OT interannual to diurnal variations (Hong et al.,
108 2008).

109   While many OT detection algorithms have been developed either using passive or active
110 remote sensing techniques, their use toward quantifying OT occurrences and attributes from
111 space are mostly from datasets with coarse spatial resolutions, e.g. ≥ 2 km for geostationary
112 satellites, 4-5 km for TRMM precipitation radar,5 km for GPM Ku radar, and 15 km for AMSU-
113 B. Spatial resolution of observations significantly influences variations of WV-IRW BTD
114 (Setvák et al., 2007) and thus influences the choice of T_b and BTD thresholds. Large spatial
115 resolution also poses challenge in identifying OTs of small size and affects the accuracy of
116 computing OT attributes such as OT area. Therefore, measurements from space with a higher
117 spatial resolution will support a better characterization of OT climatology globally, which has
118 not been derived so far.

119   The MODIS instrument (King et al., 1992) acquires data at a high spatial resolution (≤ 1
120 km) that allows to detect small OTs. This sensor has a wide view swath of 2330 km which is able
121 to take a whole picture of a mesoscale system. It is operating on both Terra and Aqua satellites,
122 overpassing the same latitude at four different times each day: around 1:30am/pm and
123 10:30am/pm equator-crossing time (ECT). In the last twenty years, both Aqua and Terra
124 satellites have a consistent equator-crossing time, making the MODIS data the longest stable
125 climate records from space.

126   To utilize these climate records, the main objective of this study is to show a near global
127   climatology of OT occurrence derived from about 20-yr Aqua and Terra MODIS data. Owing to
128   the relatively high spatial resolution of MODIS, this climatology includes OTs in small size that
129   missed by GPM radar. It includes both the tropical and mid-latitude regions, and thus makes
130   complementary to the climatology by Liu & Zipser (2005) and Hong et al., (2008) that were
131   only focused on tropical and subtropical regions. It also provides OT diurnal information at four
132   observation times. To achieve these objectives, we first develop an OT detection algorithm that
133   is specifically designed for MODIS, works for both day and nighttime data, and is more flexible
134   to thresholds compared to those used in Bedka et al. (2010) and Li et al. (2022). In sect. 2, we
135   will present the details of data and methods used for developing the OT detection algorithm.
136   Validation of the algorithm will be discussed in Sect. 3. Section 4 discusses the results produced
137   from our OT detection algorithm. Finally, in sect. 5, we conclude the findings of this study.

2. Data and Methodology

139   In order to develop a method that can detect OTs during both daytime and nighttime, this
140   study uses observations from multiple sensors onboard multiple platforms as well as a machine
141   learning method – logistic regression. The OT detection algorithm is developed in two main
142   steps. First, we manually identified a number of OT candidates from the combined CloudSat-
143   CALIPSO data. The infrared radiative characteristics of these OTs extracted from the combined
144   Aqua MODIS infrared data serve as inputs to train the logistic regression. Second, we applied
145   the regressed model to the Terra and Aqua MODIS data for automatic OT detection. We call this
146   method an *IR algorithm*.

2.1 Satellite and Reanalysis Datasets

2.1.1 CloudSat and CALIPSO

149   The CloudSat and CALIPSO satellites are two members of the afternoon constellation in
150   a sun-synchronous orbit with an Equator-crossing time at 01:30/13:30 local time (LT). The cloud
151   profiling radar (CPR) onboard CloudSat is a near-nadir-view radar operated at 94 GHz (~ 3.3
152   mm). Measuring radar reflectivity factor, the CPR probes the vertical structure of hydrometeors
153   with a minimum sensitivity of about -30 dBZ (Stephens et al., 2002, 2008). The radar's footprint
154   is 1.8 km along track and 1.4 km cross track. Its vertical resolution is 480 m with a resampled
155   resolution of 240 m. The radar is able to penetrate thick clouds and therefore is suitable for OT
156   identification as demonstrated by previous studies (Chung et al., 2008; Rysman et al., 2017;
157   Setvák et al., 2013). The radar reflectivity factor from the 2B-GEOPROF (Version P1) product
158   (Marchand et al., 2008) that shows time-height cross sections (curtains) of clouds and
159   precipitation was used for manual OT identification.

160   The CALIPSO flew about 15 s after CloudSat during the time period of observations
161   used in this work. The lidar onboard CALIPSO operates at 532 nm, having a vertical resolution
162   of 30 m below 8.2 km and 60 m above 8.2 km (Winker et al., 2003). The lidar is sensitive to
163   optically thin clouds and aerosols. The 2B-CLDCLASS-LIDAR product, provided by the
164   CloudSat Data Processing Center, reports cloud top and base heights for up to five layers (Wang
165   et al., 2012). This product utilizes the complementary features of the CloudSat radar and the
166   CALIPSO lidar, and thus includes thin cirrus clouds. The cloud top height of the topmost layer
167   was used to aid identifying OTs. Two years of 2B-GEOPROF and 2B-CLDCLASS-LIDAR data
168   (2007-2008) were used in this study.

2.1.2 MODIS

MODIS onboard both the Aqua and Terra platforms has 36 discrete spectral bands between 0.415 to 14.235 μm with spectral-dependent spatial resolutions varying between 250 m to 1 km at nadir (Barnes et al., 1998; King et al., 1992). The Aqua satellite launched in May 2002 is a member of A-Train satellite constellation. Terra was launched in December 1999 in a sun-synchronous orbit with an Equator-crossing time at 10:30/22:30 LT (Platnick et al., 2003).

To obtain OT radiative characteristics, the MODIS Collection 6.1 Level 1B calibrated radiance data, MYD021KM from Aqua and MOD021KM from Terra, were used. In this study, the bands selected have center wavelength at 6.715 and 11.03 μm for OT detection that are used for deriving brightness temperature. The uncertainties associated with these two bands are within 1% for both Terra and Aqua MODIS (Xiong et al., 2005, 2018). Navigation files with 1 km resolution (MYD03 and MOD03) were used for the geolocation information. The Aqua MODIS data from 2007-2008 were collocated to the CloudSat-CALIPSO data for selecting OT cases as a training dataset for the logistic regression model (Sect. 2.2). The Terra MODIS data from February 2000 – 2021 and the Aqua MODIS data from July 2002 -2021 were used for deriving the OT climatology presented in Section 4.

2.1.3 GPM

The Global Precipitation Monitor (GPM) core observatory, launched in February 2014, carries the first space-borne Dual-frequency Precipitation Radar (DPR) that includes a Ka-band (35.5 GHz) radar (KaPR) and a Ku-band (13.6 GHz) radar (KuPR) (Hou et al., 2014). The KuPR measures 3-D structures of convective systems with a vertical resolution of 250 m and a footprint of 5 km over a swath of 245 km. The GPM KuPR echoes have been demonstrated to be effective in the study of deep convection reaching to tropopause (Liu et al., 2020; Liu & Liu, 2016). To utilize the GPM as an independent detection of OTs, we collocated the Ku-band echoes to the OT candidates identified from Terra MODIS as a validation of our IR algorithm (Sect. 2.2). About six years (March 2014 - 2020) of data from the 2A.GPM.DPR product (V06) was used.

2.1.4 Reanalysis Data

Tropopause temperature is needed for our IR algorithm. We used the tropopause information output from the Modern-Era Retrospective Analysis for Research and Applications, Version 2 (MERRA-2), instantaneous two-dimensional collections, hourly, single-level diagnostics (MERRA2_400.inst1_2d_asm_Nx) product (Bosilovich et al., 2016). The MERRA-2 parameter 'TROPT' is a blended estimate of tropopause temperature (T_p) based on a combination of the World Meteorological Organization (WMO) definition of the primary lapse-rate tropopause (Grise et al., 2010) and equivalent potential vorticity. The tropopause data has a spatial resolution of 0.625° x 0.5° longitude-latitude. The closest MERRA-2 grid in space and time was assigned to each MODIS observation.

2.2 OT Identification Algorithm

2.2.1 OT Selections from A-Train Observations

The first step of the IR algorithm is to generate an OT training dataset. We manually selected OT candidates around the world from 2007 and 2008 by visualizing the CPR reflectivity factor from 2B-GEOPROF, topmost cloud top height from 2B-CLDCLASS-LIDAR, tropopause

210 information from MERRA-2 and the collocated T_{b11} from Aqua MODIS. For the CloudSat-
211 MODIS collocation, the nearest Aqua MODIS pixels were assigned to the CloudSat track. The
212 distance of the collocated CPR–MODIS pixels is usually less than 700 m, allowing these two
213 sensors to observe nearly the same cloud within one minute (Hong & Di Girolamo, 2020).

214 Parallax correction was examined, but not employed in this work. We found that parallax
215 correction produced nearly identical T_{b11} values as those without parallax correction. This is
216 consistent with Wang et al., (2011), who stated that the effect of parallax correction will be small
217 if the cloud object occupies a large enough area and is relatively homogeneous over the range
218 comparable to the parallax correction, which is certainly the case for the OTs being studied here.
219 Additionally, the parallax correction introduces a small amount of noise in the along-track T_{b11}
220 values due to noise in the cloud top height used in the parallax correction. The noise is sufficient
221 at times to create artifacts in our OT algorithm.

222 OTs were selected by visually inspecting the visualization rather than using a fix
223 criterion. The OT selection basically followed four principles: T_{b11} colder than T_p, cloud top
224 height above tropopause height, T_{b11} smaller than $T_{b6.7}$, and an obvious convective core. For
225 instance, Figure 1 shows an example of how we manually select OTs from this visualization.
226 Figure 1a displays that CloudSat overpassed a strong convective system with T_{b11} as low as 180
227 K. Figure 1b shows the curtain of the radar reflectivity factor from CloudSat for this convective
228 system, along with $T_{b11}/10$ (orange-solid line), cloud top height (black-solid line) and
229 tropopause information (orange-dash for tropopause temperature (T_p) divided by 10, and black-
230 dash for tropopause height) along the transect. As Figure 1b shows, in the convective core, cloud
231 top height is above the tropopause height, and the T_{b11} is colder than tropopause temperature
232 (T_p). This case is identified as an OT. In total, we have selected 209 OTs from A-Train
233 observations. Additionally, 78 non-OTs (NOTs) were also selected for model training. The
234 NOTs share very similar characteristics with OTs, i.e. T_{b11} is cold (close to or colder than T_p)
235 and has a local minimum, but no obvious convective core is observed from the visualization.
236 Supplementary 1 displays four OT and three NOT cases. Figure 2 shows very similar OT and
237 NOT T_{b11} distributions.

238 The total 287 samples were randomly distributed over four seasons and in different
239 locations on Earth. The data is available in Supplementary 2.

240

241
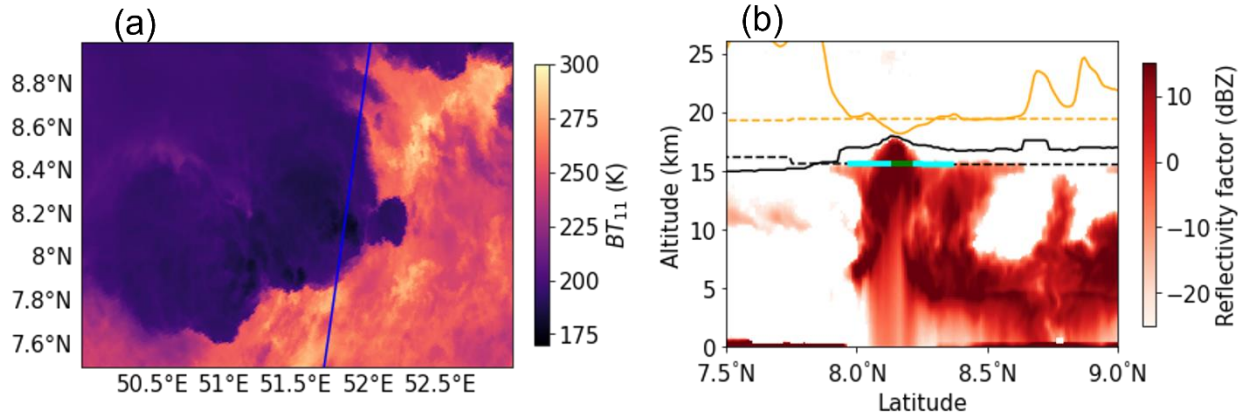
Figure 1. An OT case occurring at night over the Indian Ocean on June 1st, 2007: a) Brightness temperature at 11 μm from Aqua MODIS, with blue line indicating the CloudSat track; b) Vertical cross section of CloudSat radar reflectivity factor overlapped with MERRA-2 tropopause temperature divided by 10 (orange-dashed), tropopause height (black-dashed), topmost cloud top height from 2B-CLDCLASS-LIDAR (black-solid), and T_{b11} /10 (orange-solid). The green line in b) indicates the OT region along CloudSat track determined by the method from Marion et al. (2019), and the cyan line indicates the surrounding cirrus anvil.

2.2.2 OT Edge and Cirrus Anvil

Once an OT was manually selected from the A-Train data, OT edges were determined using the method described in Marion et al. (2019). Briefly, the local minimum T_{b11} along the CloudSat track was set as the OT center. The 1-D second derivative along two radii along CloudSat track ($\frac{d^2T_b}{dr^2}$) was computed using three-point Lagrange interpolation after Gaussian filter was applied to smooth T_{b11} field. The OT edges along the two radii are defined as the first point where $\frac{d^2T_b}{dr^2} \leq 0$. With the OT edges determined, the diameter of the OT candidate can be obtained. As an example, Figure 1b shows the OT diameter in green, indicating that this method well catches the overshooting area.

The cirrus (Ci) anvil in this work was searched within 20 pixels around the OT center but with the OT area excluded. Pixels starting from the OT edge and having $T_{b11} <$ 260 K contribute to the surrounding cirrus. A value of 260 K was used to screen cold clouds. This threshold has been commonly adopted for screening high clouds associated with deep convection (Chung et al., 2007; Tian et al., 2004). Figure 1b indicates the cirrus anvil in cyan. Once two edges of an OT and its cirrus anvil were determined, the OT center T_{b11}, the mean brightness temperature for the OT region ($\bar{T}_{b6.7}$ and $\bar{T}_{b11}$), the mean brightness temperature ($\bar{T}_{b11}$) for surrounding cirrus averaged over two radii and the tropopause temperature (T_p) for the OT case were recorded to construct the training dataset. Note that cirrus anvil is only defined in a small area within 20 km from the OT center, which is sufficient to check Tb difference between the OT and its surrounding region because OT's size is usually smaller than 15 km (Bedka and Khlopenkov, 2016). Pixels outside the 20-km radii can also contain cirrus, but do not contribute to our calculation of cirrus T_b.

273   For the 209 OT candidates, all of them have their diameters less than 25 km, 180 OTs
274   (86%) have their diameters less than 15 km, and the peak in the OT diameter distribution is about
275   10 km (Fig. 2a), being agreeable with Bedka & Khlopenkov, (2016) which states that OTs are
276   typically less than 15 km in diameter. The T_{b11} of OT center along the CloudSat track is shown
277   in Fig. 2b which displays an asymmetric U-shape distribution along latitudes. Tropical OTs tend
278   to have their center T_{b11} less than 200 K, while mid-latitude OTs tend to have center T_{b11} colder
279   than 230 K. The NOT candidates share a very similar T_{b11} distribution with OTs. We rarely
280   found OTs outside the ±60-degree latitude range. The selected OTs and NOTs are available in
281   Supplementary 2. In addition, WV-IRW BTD and T_p are two important variables used for our IR
282   algorithm.
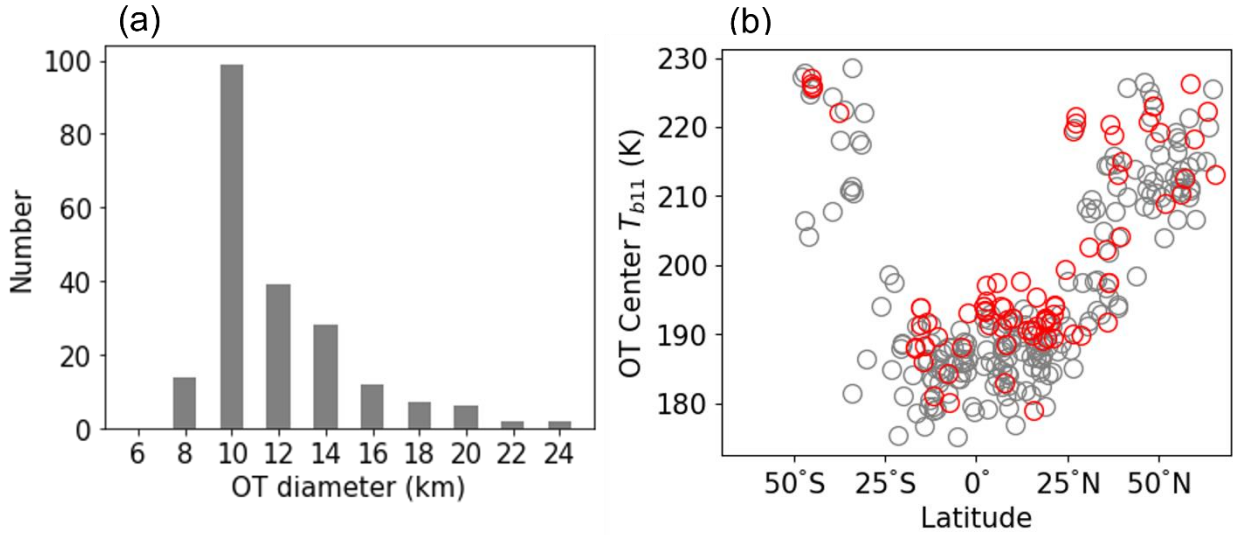
283
284   Figure 2. (a) OT diameter distribution of the 209 OT candidates selected from 2007 and 2008 A-
285   train data, and (b) brightness temperature at 11 μm of OT (grey) and NOT (red) center along
286   CloudSat track.

287

288   **2.2.3 Logistic Regression**

289   Similar to Bedka & Khlopenkov (2016), a probability was generated for an OT
290   candidate. The 209 OTs and 78 NOTs selected from A-Train observations served as inputs for
291   the logistic model. The logistic regression is a statistical model that is used to model a certain
292   event through assigning a probability between 0 and 1 such as classification of OT and NOT.
293   The logistic model depends on several variables or predictors, shown as

294    $P = \frac{1}{1+e^{-(b_0+\sum_i^n b_i x_i)}}$,   (1)

295   where P is the probability of an OT candidate, b_0 is the constant, x_i is the variable and b_i
296   represents the regressed coefficient.

297   Three MODIS-based variables were settled on after a series of tests to optimize the
298   accuracy. They are x_1- the difference between Ci anvil mean T_{b11} and OT center T_{b11}, x_2- the
299   difference of T_p and OT center T_{b11}, and x_3- the difference of mean $T_{b6.7}$ ($\bar{T}_{b6.7}$) and mean T_{b11}

300 ($\bar{T}_{b11}$) of OT. 156 OTs and 48 NOTs were used to train the model and the regressed results are
301 summarized in Table 1. The total accuracy is about 84% when probability > 0.6 is predicted to
302 be an OT. 53 OTs and 30 NOTs were used to validate the regressed model with a total accuracy
303 about 82%. We have tested the accuracy as a function of sample size and found a stable model
304 accuracy of ~84% when total sample size is larger than about 150, indicating that total samples
305 of 287 should be sufficient for training a robust model in our study.

306   Table 1. A summary of the regressed coefficients for the variables selected for OT
307 detection used in Equation 1.

Variables	Coefficients for the variables[*] (constant = -3.2397 ± 0.753)
x_1- difference between Ci mean T_{b11} and OT center T_{b11}	0.2075 ± 0.053
x_2- difference of tropopause T_p and OT center T_{b11}	0.3516 ± 0.085
x_3- difference of averaged OT $T_{b6.7}$ and averaged OT T_{b11}	0.4996 ± 0.188

308 * The Logistic Regression is based on python module – Statsmodels. The p values for the
309 regressed coefficients are smaller than 0.008 based on z-test. The uncertainties for each
310 coefficient are represented by standard errors.

311 **2.2.4 Application of IR Algorithm to MODIS**
312

313   The logistic regression in Sect. 2.2.3 forms the basis of our IR algorithm, which aims to
314 automatically identify OTs from Terra and Aqua MODIS in the daytime and at nighttime. The
315 application of the IR algorithm starts from pixel search with T_{b11} colder than T_p, and T_{b11} less
316 than 200 K in the tropics (within 25° latitude) or less than 230 K in the midlatitudes (outside 25°
317 latitude). These T_{b11} thresholds selected to ensure that all OTs identified in Fig. 2b would pass
318 this first OT candidate selection criteria. If the pixel passed these thresholds and is a local
319 minimum in T_{b11} field in a 41 km x 41 km window, we continued to find the OT edges in eight
320 directions using the method by Marion et al. (2019), as mentioned in Sect. 2.2.2. $\bar{T}_{b11}$ and $\bar{T}_{b6.7}$
321 of the OT area are further computed over the pixels along eight radii once OT edges have been
322 determined. $\bar{T}_{b11}$ of the surrounding cirrus is also computed in eight directions in the cirrus area
323 as defined in Sect. 2.2.2. When the surrounding cirrus $\bar{T}_{b11}$ is warmer than OT center T_{b11} and
324 this OT case shows positive WV-IRW BTD (i.e. $\bar{T}_{b6.7} - \bar{T}_{b11} > 0$), OT probability is calculated
325 according to the logistic regression from Sect. 2.2.3. If one of the mentioned conditions does not
326 satisfy, the algorithm will search for next pixel. The flowchart of the IR algorithm application is
327 summarized in Fig. 3.

328   The window size of 41 km was adopted considering that 98% of the OTs (Fig. 2) have
329 their diameters less than 20 km according to A-Train observations (Sect. 2.2.2). This window
330 makes sure that two OT centers are at least 20 km apart and that enough pixels contribute to the
331 cirrus anvils. If multiple OTs occurred in the same window, the one with the coldest T_{b11} was
332 selected.
333
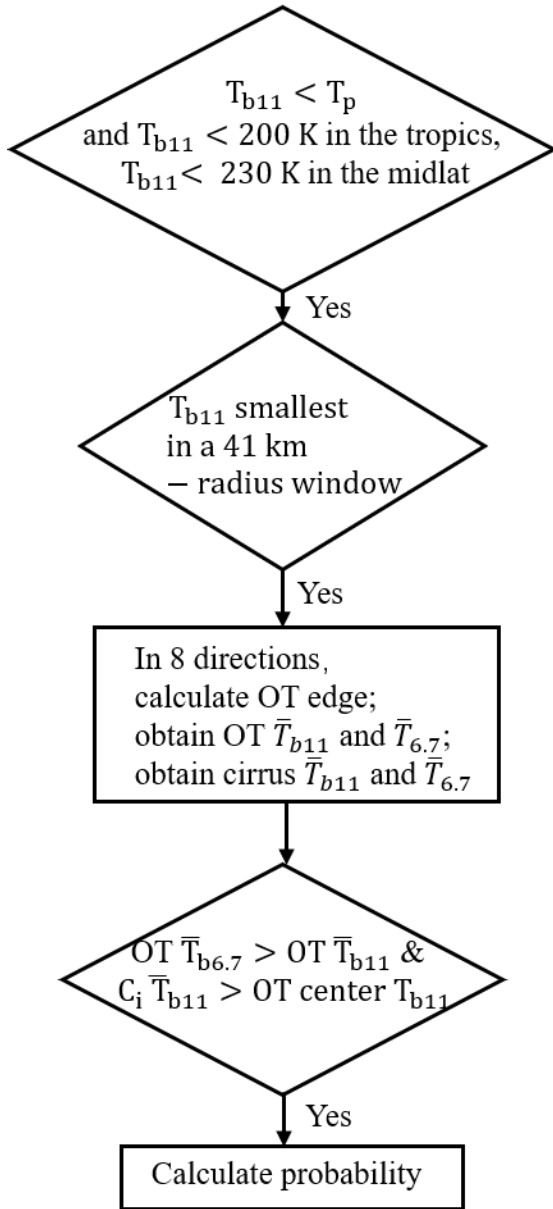
334
335
336   Figure 3. Flowchart for the application of IR algorithm to MODIS data. The $\bar{T}_b$ represents the
337   mean of brightness temperature.

338
339   **3. Validation of OT Detection Algorithm**
340   **3.1 Comparison with GPM**
341   GPM has been demonstrated to be an effective tool in studying intense storms and
342   overshooting top events (Hourngir et al., 2021; Liu et al., 2020; Liu & Liu, 2016). Here, we used
343   the GPM observations for two purposes: To compare the performance of OT detection between
344   GPM KuPR and Terra MODIS, and to investigate the cloud structure of detected OTs. The
345   colocation between GPM KuPR and MODIS data was achieved when the time difference
346   between them was within 5 minutes and the spatial difference between them was less than 10
347   km. A 5-minute time window was used because the life cycle of OTs can be as small as several

348   minutes (Setvák et al., 2013). The collocating process was performed only when OT candidates
349   were identified from Terra MODIS. We obtained 6949 colocations for the period of March 2014
350   – December 2020.

351   Ku-band radar reflectivity factor (Ze) in an area with a radius less than 40 km around the
352   colocated radar pixel were collected to construct the contour frequency by altitude diagram
353   (CFAD; Yuter & Houze, 1995). The parallax error between KuPR and MODIS could be more
354   than 20 km according to the method described in Wang et al. (2011). Also, OT diameter is likely
355   less than 20 km. An area with a 40 km radius for the collocated KuPR data is likely able to
356   encompass the OT event identified by MODIS. Figure 4 shows the CFADs contributed by all
357   (6949) collocated OT cases. The CFADs were segregated into 5 OT probability intervals for the
358   tropical and mid-latitude areas. As shown, the largest frequency occurs above 5 km in tropical
359   areas (Figs. 4a1-a5). As the OT probability increases, the frequency increases for large Ze (> 30
360   dBZ) below 5 km. In the midlatitudes (Figs. 4b1-b5), higher frequency of the Ze occurs below 5
361   km when OT probability is less than 0.85. For those OT cases with P > 0.85, large frequency is
362   mostly above 5 km, and large Ze (> 30 dBZ) occurs more frequently below 5 km. With an
363   analysis of DPR rain type product, we noticed that the large Ze (e.g. > 30 dBZ) below 5 km tend
364   to associate with convective rain in both the tropics and midlatitudes. An increase of convective
365   rain in the CFADs with larger OT probability indicates more likely OT occurrence. These
366   CFADs demonstrate that the probability generated from our IR algorithm indicates storm
367   intensity and a confidence level of OT detection.

368
369
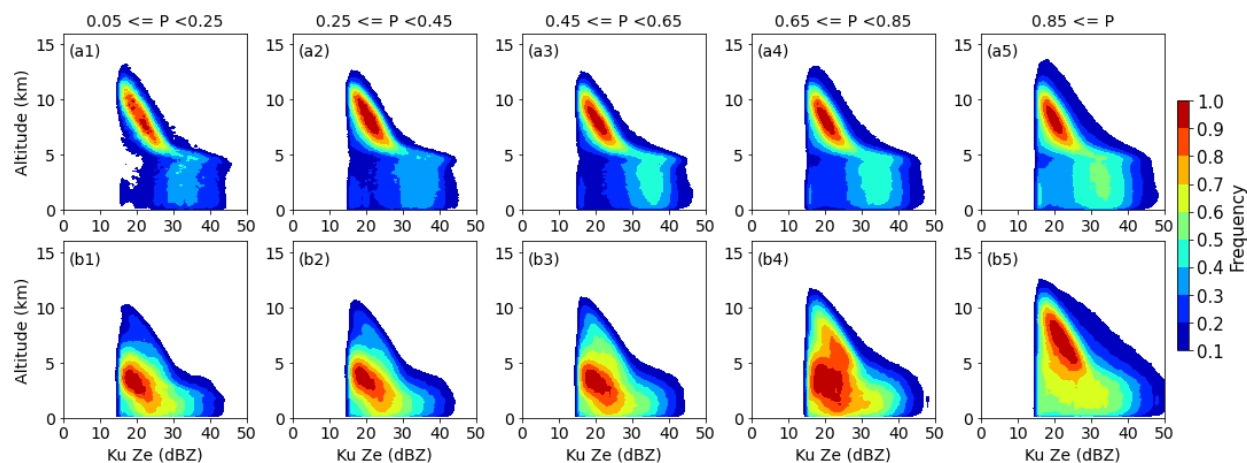
370
371   Figure 4. Contoured frequency by altitude diagram, showing the frequency normalized by the
372   maximum bin of radar reflectivity. Data were binned at 1dBZ intervals at each level. The upper
373   panels are for the tropics (within 25° latitude), and the lower panels are for the midlatitudes
374   (between 25° and 60° latitude).

375

376   To compare the performance of OT detection between GPM and MODIS, we need to
377   determine when GPM detects an OT. If the maximum altitude of 15 dBZ in the 40-km radius
378   area was higher than 2 km below the MERRA-2 tropopause, an OT flag was assigned to the
379   collocated GPM pixel. Previous studies also adopted a level below the tropopause as the OT

380   reference considering the tropopause height variability (Sun et al., 2019; Zhuge et al., 2015) such
381   as the noted double tropopause observed in deep convection (Vergados et al., 2014). Here, 2 km
382   was selected due to an agreement of 67% between MERRA-2 and ERA-5 tropopause height
383   (from ECMWF-AUX (Partain, 2007)) for the 287 OTs and NOTs cases used in Sect. 2. Once OT
384   flags were assigned to the collocated GPM cases, agreement of OT detection between MODIS
385   and GPM was calculated for a wide range of OT probability generated by the IR algorithm. The
386   agreement is expressed as

387
$$Agreement = \frac{N(H > H_p - 2 \cap P_1 < P < P_2)}{N(P_1 < P < P_2)} \quad (2)$$

388   where H is the maximum altitude (in km) of 15 dBZ in the 40-km radius aera, H_p is tropopause
389   height from MERRA-2, and N is the OT numbers with OT probability between P1 and P2.
390   Figure 5 shows the agreement in OT detection between MODIS and GPM which
391   increases with OT probability. In the tropics, the agreement is about 70% when P > 90% with
392   enough samples, while in the midlatitudes, the agreement is larger than 80% when P > 0.90.
393
394
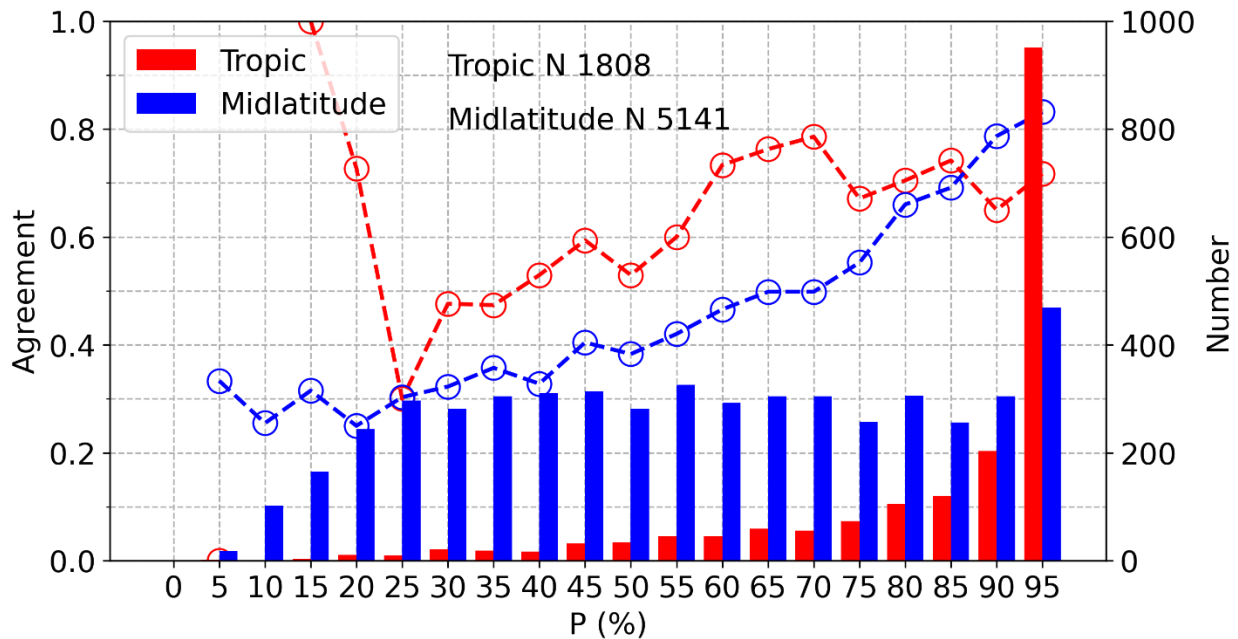
395

396   Figure 5. Comparison of OT detection between GPM and Terra MODIS. Curves represent
397   agreement of OT detection between MODIS and GPM in various probability intervals, red for
398   the tropics and blue for the midlatitudes; the numbers of potential OT candidates are shown in
399   bars. N stands for sample number.

400
401   **3.2 Manual Check**
402   As a complement to GPM-MODIS comparison for assessing IR algorithm accuracy, we
403   manually checked 1158 daytime OT candidates (selected randomly across the year) from Terra
404   MODIS from 2018-2020 (data is available is Supplementary 3). These OT candidates are with a
405   wide range of probability. OT and NOT flags were assigned to the candidates by visually

406   inspecting the IR and visible images from the NASA Worldview website
407   (https://worldview.earthdata.nasa.gov). The fraction of OT and NOT segregated at a 0.1
408   probability (generated from the IR algorithm) interval was calculated (Fig. 6). As displayed, the
409   fraction of OT substantially increases when the probability is greater than 0.8 in both the tropics
410   and midlatitudes. In the tropics, the fraction of NOT is about 30% when P is between 0.8 and
411   0.9, and it decreases to about 10% when P ≥ 0.9. In the midlatitudes, when the P is small (e.g. <
412   0.8), NOT fraction is higher than OT fraction. Only when P ≥ 0.9, NOT fraction drops to about
413   10%. With a manual check of about 900 OT candidates selected from July, 2018 Aqua MODIS,
414   similar accuracy was obtained (~ 90% when P ≥ 0.9). This manual check is consistent with the
415   OT comparison with GPM as discussed in Sect. 3.1, i.e., higher OT probability gives higher
416   confidence in our IR algorithm for OT detection.
417
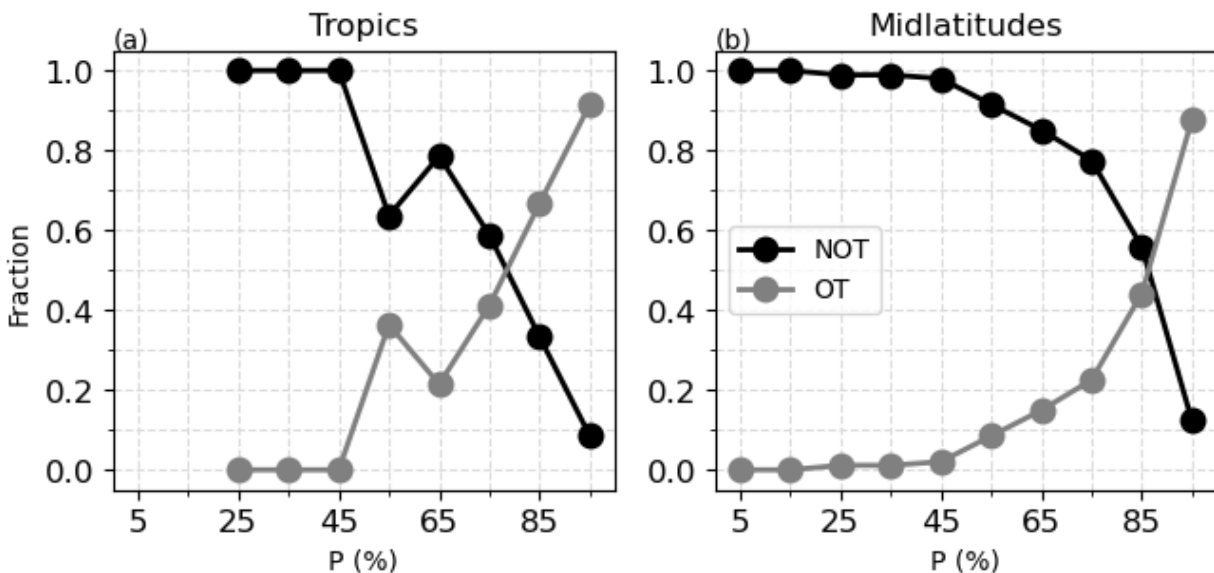
418
419   Figure 6. Fraction of OT candidates with a wide range of probability in the Tropics (a), and
420   midlatitudes (b). X-axis shows in a probability interval of 0.1.
421
422   Overall, we choose a P threshold of 0.9 in both the tropical and mid-latitude regions,
423   which ensures a total detection accuracy of ~ 0.9 (better than 0.9 in the tropics and slightly lower
424   than 0.9 in the midlatitudes) as demonstrated in Sect. 3.2. For the Terra MODIS data from
425   February 2000 to December 2021 and Aqua MODIS data from July 2002 to December 2021, OT
426   candidates that pass the probability threshold of 0.9 account for about 30% and 35%,
427   respectively, of all candidates over regions within 60°S - 60°N. In the tropics, 58% (62%) of the
428   candidates from Terra (Aqua) MODIS have P > 0.9, while in the midlatitudes, only 13% (16%)
429   of the candidates were retained. Note that we do not consider polar regions because our manual
430   selected OTs in Sect. 2.2 rarely occur outside 60° latitudes.

431   **4. Results and Discussions**

432   In this section, we show an OT climatology of those OT candidates with P ≥ 0.9.
433   Candidates with P < 0.9 were excluded due to a high fraction of NOTs as discussed in Sect. 3.

434   **4.1 Case Analysis**

435   Before showing the climatology, we first show four cases including all OT candidates
436 with a variety of probabilities for a detailed view of the performance of our IR algorithm in
437 different storm environments.

438   Figure 7 shows visible reflectance overlapped with OT centers, which are colored by OT
439 probability. T_{b11} for each case is also shown overlapped with the pixels colder than tropopause
440 and having positive WV-IRW BTD (marked in white). The rain type and precipitation rate
441 averaged between 2-4 km from GPM are shown in the third and fourth columns.

442   Overshooting tops in tropical cyclones (TC) are common. They are found closely linked
443 to intense convection and rapid intensification in TCs (Griffin, 2017; Monette et al., 2012; Tao
444 and Jiang, 2013). Figures 7a1-7a4 displays a tropical cyclone over the north Indian Ocean on
445 Nov. 08th, 2019. OTs are detected in the area with very cold T_{b11} associated with strong
446 convection and precipitation as GPM identifies convective rain type near OT areas. Our
447 algorithm usually generated high probability for OT candidates detected in TCs.

448   In the mesoscale convective system case (Figs. 7b1-b4), OTs are detected in the clusters
449 that associate with cold T_{b11} and positive WV-IRW BTD. Strong precipitation is indicated by
450 GPM. Our algorithm also usually produces high probability for OTs detected in mesoscale
451 convective systems.

452   Cold air outbreaks can produce shallow convection when cold air blows from frozen
453 surfaces to warmer ocean. The Cold-Air Outbreaks in the Marine Boundary Layer Experiment
454 (COMBLE) found that these convective clouds are commonly lower than 5 km associated with
455 updrafts of 4-5 m s^{-1} (Geerts et al., 2022). In the cold air outbreaks, the tropopause is low, which
456 is often at a level below 500 hPa (Papritz et al., 2019; Terpstra et al., 2021), compared to the
457 mid-latitude tropopause climatology of 200-300 hPa (Wilcox et al., 2012). Thus, updrafts in
458 these shallow convective clouds are able to penetrate the tropopause and produce overshooting
459 cloud tops. In the third case (Figs. 7c1-c4), overshooting tops from convective turrets over the
460 north Atlantic within a cold air outbreak occur with high OT probability. GPM identifies
461 convective precipitation surrounding by stratiform precipitation in these shallow convective
462 clouds. Our method allows for the detection of these OTs that can occur in unstable conditions
463 with shallow tropopauses.

464   Mid-latitude winter cyclones are associated with mostly stratiform cloud systems
465 (Stewart et al., 1998), as also demonstrated by the GPM rain type that shows mostly stratiform
466 precipitation (Figs. 7d1-d4). The tops of stratiform clouds associated with the fronts usually
467 reach to tropopause without strong convective cores. However, they can occur associated with
468 lightning and heavy precipitation when fueled by potential instability, with updrafts of 6-8 m s^{-1}
469 (Murphy et al., 2017; Rauber et al., 2014, 2015). Our algorithm detects OT candidates in this
470 cloud system usually with low probability which will be excluded in our OT climatology
471 analysis except for some rare situations with high OT probability.

472

473

474
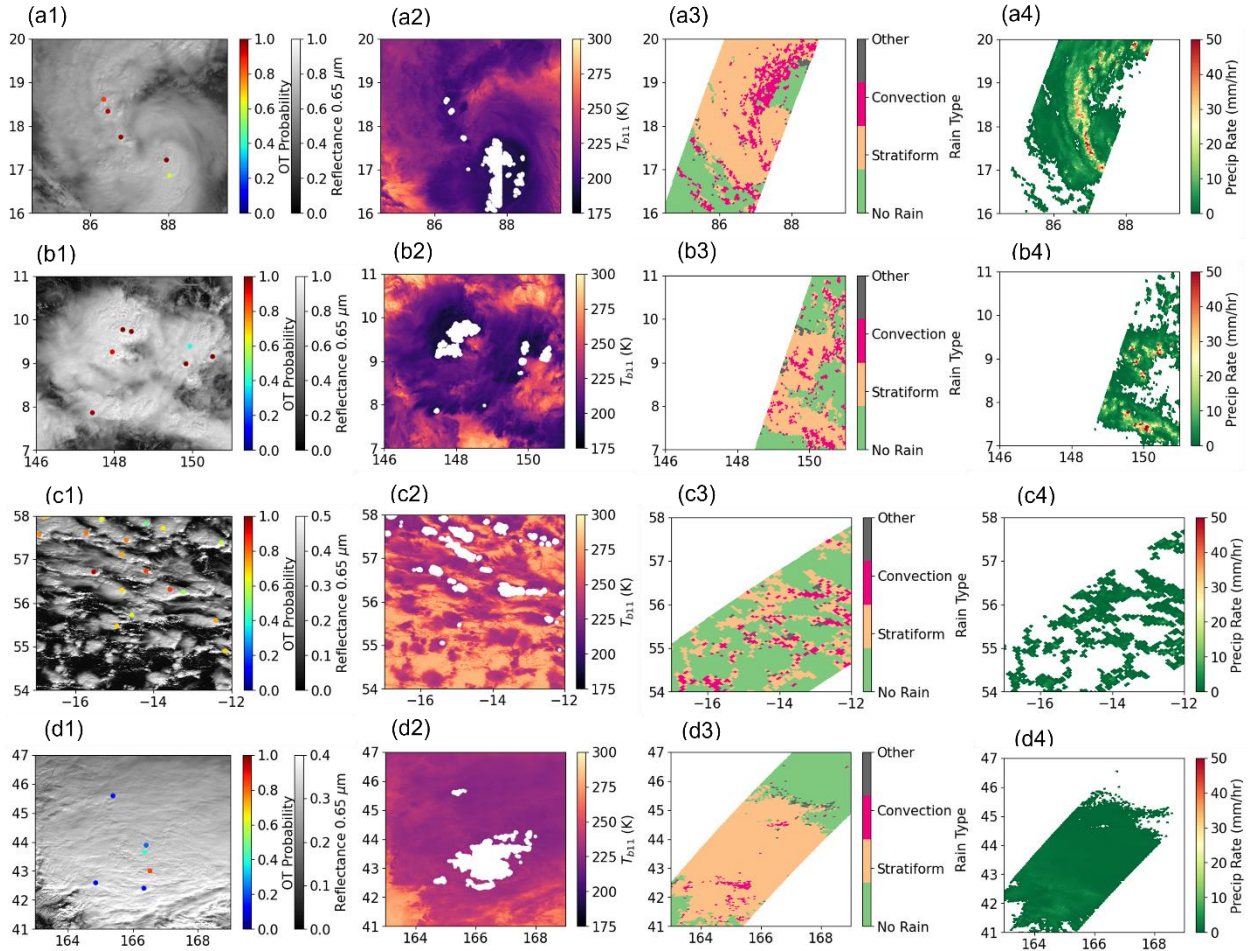
Figure 7. Four selected cloud systems with OTs detected by our IR algorithm. First column shows the reflectance at 0.65 μm (dots indicate OT probability), the second column shows the brightness temperature at 11 μm (white dots indicate pixels colder than tropopause temperature and having positive WV-IRW BTD). Columns 3 and 4 represent rain type and precipitation rate from GPM, respectively. Case 1 (a1-a4) is for the tropical cyclone over Bay of Bengal on Dec. 8th, 2019, case 2 (b1-b4) is for a mesoscale convective system over East of Philippines on Dec. 03rd, 2019, case 3 (c1-c4) (Mar. 10th, 2019 over the north Atlantic Ocean) is for shallow post-frontal convection, and case 4 (d1-d4) (Dec. 15th, 2018 over the north Pacific Ocean) is for the cloud system in the midlatitude cyclone.

4.2 Near Global OT Distributions

Figure 8 shows the seasonal distributions of OT occurrences contributed by those OT candidates with P ≥ 0.9, derived from Terra (February 2000 - 2021) and Aqua (July 2002 -2021) MODIS. As displayed, OT distributions and their seasonal variations follow the expected pattern based on the known climatology of convection (Alcala and Dessler, 2002; Funk et al., 2015). In JJA (Fig. 8b), as revealed by both Aqua and Terra MODIS, OTs primarily distribute over north of the equator in the intertropical convergence zone (ITCZ). A large population of OTs over India, Bay of Bengal, and southeast Asia are associated with the summer South Asian monsoonal

494 system. Our algorithm also detects considerable OTs in Asia between 45°-60° latitudes and in
495 Europe, where severe storms occur in local summer (Groenemeijer et al., 2017; Shikhov et al.,
496 2021). These profound OTs agree with what GPM has found in the northern mid and high
497 latitudes (Liu et al., 2020). However, a T_{b11} threshold of 215 K usually filter out these OTs (e.g.
498 Li et al., 2022). Another hot spot of OTs occurs in central North America. In addition, we
499 observe a narrow belt of large OT occurrences over the west Atlantic Ocean, which are
500 associated with the location of tropical cyclones.

501 Aqua MODIS also shows frequent OT occurrences over the southeastern United States
502 associated with the afternoon convection. In regions over the U.S. southwest and northwestern
503 Mexico, OTs are detected associated with the summer North America Monsoon (Adams and
504 Comrie, 1997).

505 During DJF (Fig. 8d), OT occurrences are about 44% at 10:30 LT (Terra equator crossing
506 time) and 36% at 1:30 LT (Aqua equator crossing time) ((Nsummer-Nwinter)/ Nsummer) less
507 than that in JJA. OTs are primarily located over the Southern Hemisphere as the ITCZ moves to
508 the south of the equator. A large number of OTs are detected by Aqua MODIS over tropical and
509 subtropical South America and Africa. In the Northern Hemisphere, OTs become infrequent over
510 land. Note that ice clouds have an occurrence frequency about 70% over mid- and high-latitude
511 Asia during winter (e.g. Hong and Liu 2015), which often pose challenges for OT identification.
512 These cold ice clouds are rarely classified as OTs in our analysis, demonstrating the ability of
513 our IR method to avoid the misclassification of cold ice clouds to OTs. In contrast, over the mid-
514 latitude ocean in winter, we see some OT occurrences. These OTs are associated with isolated
515 convective clouds occurring in the cold air outbreaks as discussed in Sect. 4.1. These OTs are
516 also observed over Southern Ocean during JJA (Austral winter). We also notice a small number
517 of OTs extending from northwest to southeast North America in DJF. These OTs are associated
518 with the convection in winter mid-latitude cyclones as discussed in Sect. 4.1.

519 Convective activity over land is weak at Terra overpass time in the morning (~ 10:30 am)
520 and it becomes more frequent and intense in the afternoon when Aqua satellite overpasses. This
521 is revealed by the differences of OT occurrences between Terra and Aqua, indicating the
522 variability of OT diurnal cycles.

523

524

525
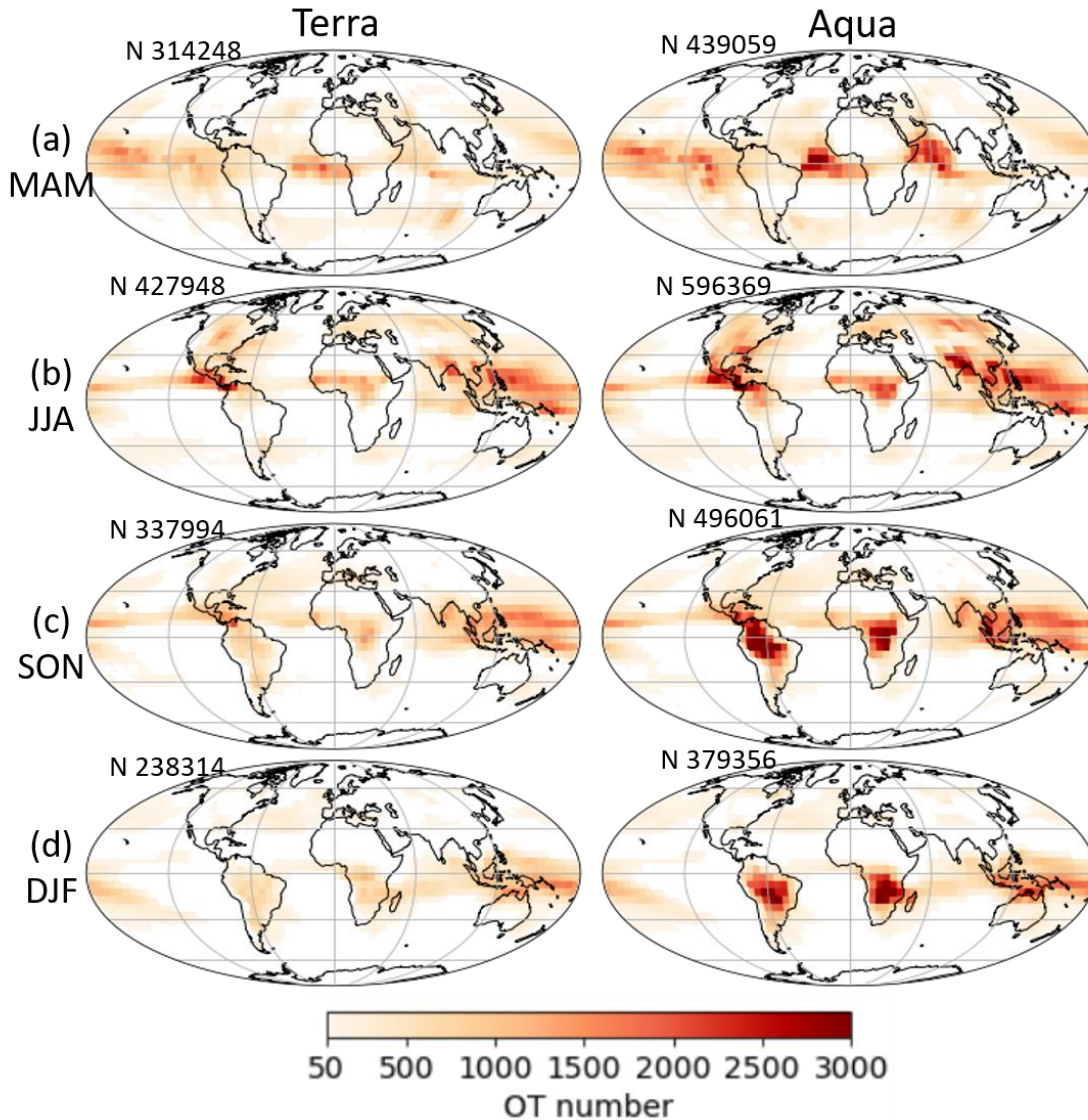
Figure 8. The global distributions of OT occurrences derived from Terra and Aqua MODIS in four seasons: (a) March-April-May (MAM), (b) June-July-August (JJA), (c) September-October-November (SON) and (d) December-January-February (DJF). Grid resolution is 5° longitude by 5° latitude. Samples in grids less than 50 are shown in white. N over the upper right corner in each panel stands for sample number.

4.3 OT Diurnal Cycle

This section discusses OT diurnal cycles based on the four observation times by Aqua and Terra MODIS. The OT occurrences in the daytime (~10:30 am and ~1:30 pm) and at night (~10:30 pm and ~1:30 am) are displayed in Fig. 9. According to previous studies on the diurnal cycle of convection (Alcala and Dessler, 2002; Nesbitt and Zipser, 2003), convective activity over land is generally more frequent and intense in the afternoon and evening compared with early morning. Over oceans near the coastlines, morning convection is more intense (Johnson,

540   2011). In agreement with previous studies, we observe the most OT occurrences at about 1:30
541   pm from Aqua MODIS, primarily contributed by land areas including tropical South America,
542   tropical Africa, the Maritime continent and the southern foothills of Himalayas. Over Bay of
543   Bengal, South China Sea, Gulf of Guinea, Gulf of Mexico, Panama and its surrounding regions,
544   OTs away from coastlines have been observed, commencing in the morning (~ 10:30 am) and
545   continuing into afternoon (~ 1:30 pm). Over the west Pacific Ocean, OTs occur the most around
546   midnight at ~ 1:30 am.

547   To better view the OT diurnal cycles, Figure 10 shows when maximum and minimum OT
548   occurrences occur in the four-observation time. Diurnal cycle intensity defined by the difference
549   of maximum and minimum OT numbers normalized by the mean is shown in Figs.10 e and f. As
550   expected (Figs. 10a and 10b), the largest OT occurrences over land occur at about ~ 1:30 pm
551   except for central North America and west Africa where have a midnight maximum in
552   convection during JJA (Janiga and Thorncroft, 2014; Nesbitt and Zipser, 2003; Tian et al., 2005).
553   Ocean areas consistently have maximum OT occurrence at ~ 1:30 am (Figs.10a and 10b). The
554   minimum OT occurrence over land usually occurs at ~ 10:30 am except for some regions over
555   North America and Asia where the minimum OT occurrence is at ~1:30 am during JJA (Fig.
556   10c). The time for minimum OT occurrence over ocean has a large variability.

557   The diurnal cycles of OT occurrences over ocean are generally weak (Figs. 10e and 10f),
558   being consistent with previous convection diurnal cycle analysis (Alcala & Dessler, 2002; Liu &
559   Zipser, 2005; Nesbitt & Zipser, 2003). In contrast, the OT diurnal cycles over land are much
560   stronger than over ocean. Strong regional variations are also discovered over land areas.
561   Relatively strong OT diurnal cycles are found during JJA over southwest North America,
562   southeast United States, Tibetan High, tropical South America, and during DJF over southeast
563   Australia, tropical and subtropical South America and subtropical Africa. Relatively weak
564   diurnal cycles over land are observed in central North America and west Africa in JJA. Strong
565   regional variations in OT diurnal cycle over land are consistent with previous studies based on
566   convection and precipitation that demonstrate the diurnal cycles are complicatedly modulated by
567   land-sea contrast, topography, coastline curvature and response to solar heating to surface
568   (Janiga and Thorncroft, 2014; Tian et al., 2005).

569

570
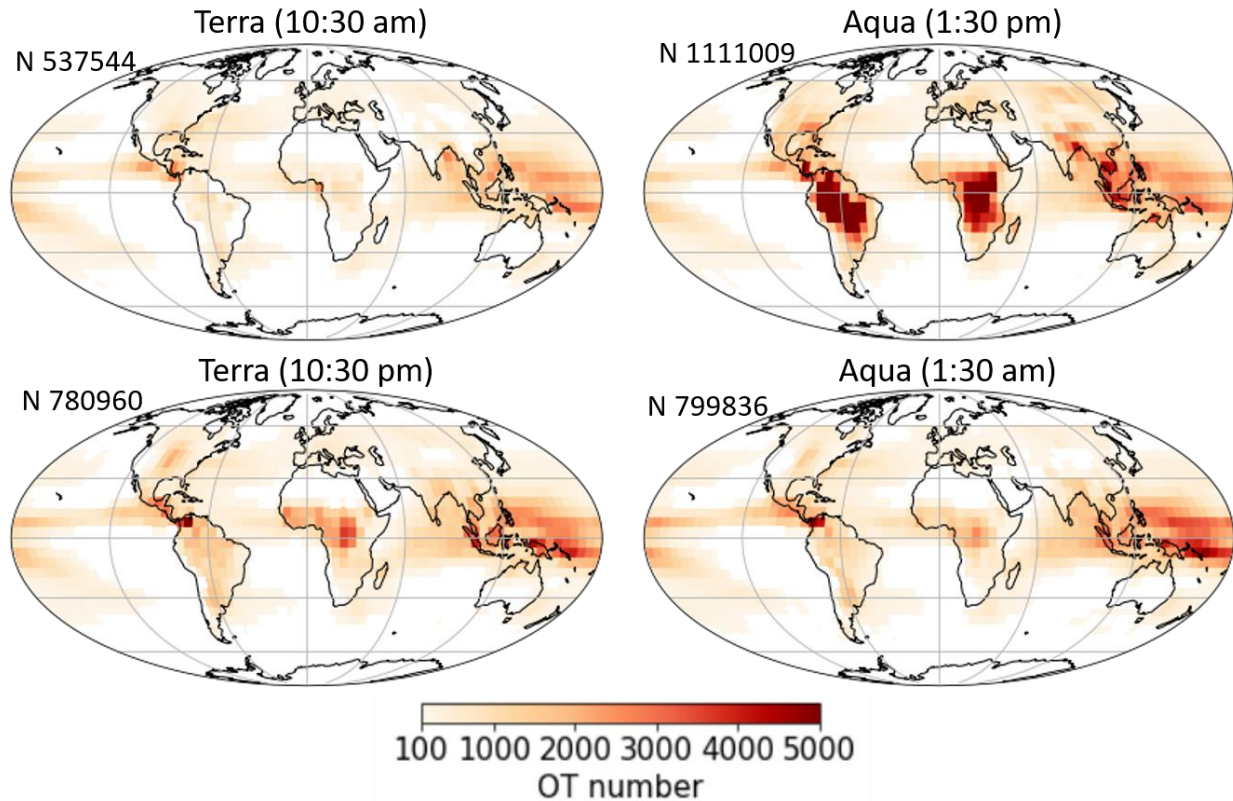
Figure 9. The global distributions of OTs at four observation times. Grids with OT number < 100 are shown in white. N stands for sample number.

573
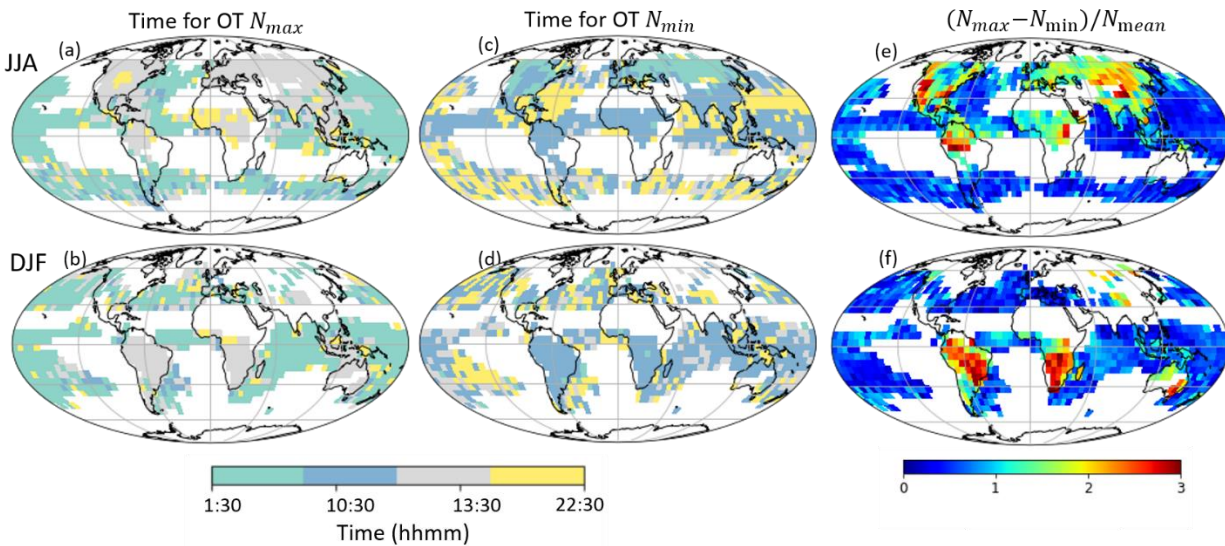
Figure 10. Panels a-d are for the time when maximum and minimum OT occurrence occurs across the four-observation time. Panels e-f are for diurnal intensity of OT occurrences, defined as the difference of maximum and minimum OT occurrences, normalized by the mean. Only when the minimum OT occurrences > 10 in each 5°x5° grid, data is shown.

578 **4.4 Land-Sea Contrast**

579   From the diurnal cycle analysis in Sect. 4.3, we have noticed some land-sea contrast in
580 OT characteristics. For instance, OTs occur more frequently in the afternoon over land, whereas
581 they are more frequent at midnight over ocean, and OT occurrence diurnal cycle is stronger over
582 land than over ocean. In this section, attention is placed on OT center T_{b11}, which indicates
583 storm intensity. By checking the geospatial distributions of OT center T_{b11}, we observe
584 extremely cold OT center T_{b11} (e.g. < 180 K) appearing over the tropical regions, including
585 regions near northern Australia, east of Papua New Guinea, India and nearby Arabian sea,
586 tropical and subtropical Africa, and tropical and subtropical South America, derived from both
587 Aqua and Terra MODIS (Figs. 11a and 11b). The locations of cold OTs are also aligned with the
588 places where occur intense convection based on TRMM (Zipser et al., 2006).

589   Particularly, the first 10 coldest OTs (marked in red triangles and summarized in Table 2)
590 from Aqua and Terra MODIS nearly occur in Sothern Hemisphere with more cases over land
591 than over ocean. The top 10 coldest OTs from Aqua are colder than 167 K with the coldest OT of
592 165.6 K over east of Papua New Guinea, whereas Terra shows the coldest OT of 167.2 K
593 occurring in northern Australia. This finding agrees with the cold OT distributions discussed in
594 Proud & Bachmeier, 2021, which states that an extremely cold tropopause coupled to an
595 energetic overshooting top produced such a cloud top temperature.

596   Additionally, Figs. 11a and 11b reveal colder OTs over land than over ocean at the same
597 latitudes. By checking the probability density distributions (PDFs) of OT center T_{b11}, we find
598 that land-sea contrast in OT T_{b11} also relies on diurnal cycle. In the daytime morning (~ 10:30
599 am) when convection over land is weak, T_{b11} over land is slightly warmer than over ocean in
600 both the tropics and midlatitudes (Figs. 11c and 11e). Land-sea contrast in T_{b11} is small at this
601 time. At ~1:30 pm as convection becomes stronger over land, T_{b11} over land is on average 0.8 K
602 and 2.3 K colder than over ocean in the tropics and midlatitudes, respectively (Figs. 11c and
603 11e). At nighttime (Figs. 11d and 11f), land-sea contrast in T_{b11} becomes stronger than in the
604 daytime. In the tropics, T_{b11} over land is about 1 K on average colder than that over ocean,
605 whereas in the midlatitudes, it is about 2 K colder over land than over ocean.

606   Our findings indicate that OTs over land are more intense than over ocean except for the
607 early morning (~ 10:30 am) when convection over land is weak. These findings agree with
608 previous studies that have shown more intense convection over land area, associated with
609 stronger updrafts than the oceanic counterpart (Jeyaratnam et al., 2021; Liu & Zipser, 2005).

610
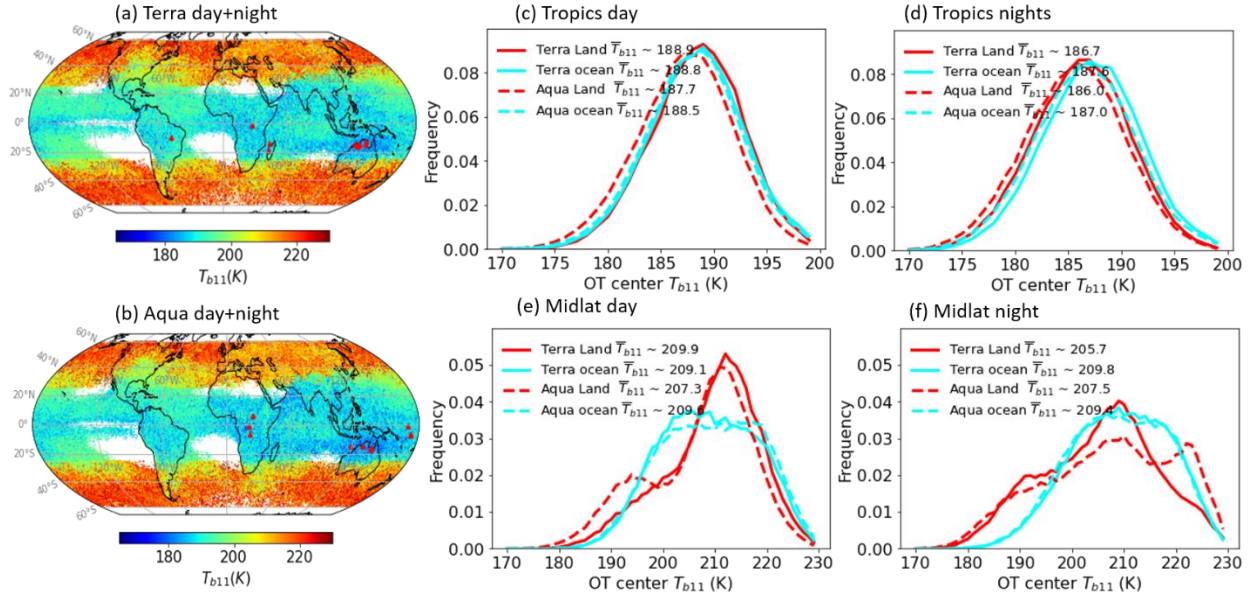
Figure 11. a and b are for spatial distributions of OT center T_{b11}. Red triangles indicate the locations of top ten coldest OTs. Panels c-f are for OT center T_{b11} PDFs in the tropics and midlatitudes, segregated in day and nighttime.

Table 2. Summary of the top 10 coldest OTs from Terra and Aqua, respectively.

	Terra				Aqua			
	$T_{b11}(K)$	Location(lon,lat)	Time[1]	D/N [2]	$T_{b11}(K)$	Location(lon,lat)	Time	D/N
1	167.2	129.75,-14.54	2016365.1350	N	165.6	172.65,-6.66	2018365.1415	N
2	167.6	128.62,-15.76	2006023.1410	N	166.4	169.81,-0.99	2018365.1410	N
3	167.6	125.47,-14.62	2014004.0205	D	166.5	21.34,-0.74	2015082.0030	N
4	167.8	27.28,-1.46	2013023.2020	N	166.6	22.29,-6.15	2020053.2355	N
5	167.8	-48.54,-9.98	2013029.0130	N	166.7	172.54,-7.35	2018365.1415	N
6	167.8	136.12,-14.72	2019003.1320	N	166.7	138.75,-17.12	2018332.0420	D
7	167.8	44.58,-19.05	2006074.1935	N	166.8	138.71,-15.78	2012080.1625	N
8	168.1	44.63,-13.74	2004023.1925	N	166.8	129.75,-14.64	2003020.0500	D
9	168.3	135.39,12.79	2008006.1405	N	166.9	118.45,-14.93	2016359.0600	D
10	168.3	128.49,-16.31	2018001.1405	N	166.9	24.93,5.63	2008123.1140	D

1.Time in the format of year.day.hhmm

617   2.D for day and N for night

618

5. Conclusions

620   To utilize about two-decade MODIS records in study of convective overshooting tops,
621   we developed an IR algorithm to detect OTs from MODIS. The resultant OT climatology was
622   used to understand OT regional and seasonal distributions, OT diurnal cycles and OT land-sea
623   contrast.

624   The approach to detect OTs uses IR radiances from MODIS water vapor (6.7 μm) and
625   window (11 μm) channels. This approach was built upon the logistic regression which was
626   trained and validated with ~ 287 OT candidates identified from the combined CloudSat-
627   CALIPSO-MODIS (CCM) data. As demonstrated by six-year collocated GPM observations, the
628   OT probability generated by the IR algorithm indicates storm intensity and represents a
629   confidence level of OT detection. When OT probability is higher than 0.9, the accuracy for OT
630   detection is better than about 0.9 as validated by manual check.

631   The global and seasonal distributions of OT occurrences follow the expected pattern
632   based on the known climatology of deep convection and precipitation, shifting with the ITCZ
633   and monsoonal systems. Frequent OTs are also observed over central North American, Europe,
634   northern Asia and the northwest Atlantic Ocean in summer. Our OT climatology also includes
635   those OTs observed in the shallow convection over the mid-latitude ocean during spring-winter
636   cold air outbreaks.

637   MODIS observations at four different times were used to derive part of the OT diurnal
638   cycle. The diurnal cycle follows the known diurnal cycle of convection: The most OT
639   occurrences are observed at about 1:30 pm (ECT) over most land area, including tropical and
640   subtropical South America, tropical and subtropical Africa, southeast North America, foot of
641   Himalayas and Maritime continent, etc. Over ocean, maximum OT occurrences are usually at
642   around midnight (~1:30 am) except for offshore ocean. OT occurrences in the morning (~ 10:30
643   am) over coastal ocean are apparent which continue to the afternoon at ~ 1:30 pm. Minimum OT
644   occurrences are usually at ~10:30 am over land. Over ocean, however, minimum occurrences
645   can be at any time except 1:30 am. Also, the OT diurnal cycle is stronger and more varied over
646   land than over ocean.

647   Jeyaratnam et al., (2021) indicated that tropical convection is deeper than mid-latitude
648   convection. This is also revealed by the midlatitude-tropics contrast in OT center T_{b11} shown in
649   this study, i.e. tropical OTs are colder than mid-latitude OTs. In the tropics, the OT center T_{b11}
650   tends to be colder over land than over ocean except at ~ 10:30 am when convection over land is
651   weak. Also, the top 10 coldest OTs from either Terra or Aqua mostly occur over land. These
652   results agree with previous studies that have confirmed that tropical land areas exhibit more
653   intense overshooting convection than the tropical oceans (Alcala & Dessler, 2002; Liu & Zipser,
654   2005). Mid-latitude OTs have stronger land-sea contrast in T_{b11} than in the tropics with OTs over
655   land being 2.3, 4.1 and 1.9 K colder than that over ocean at about 1:30 pm, 10:30 pm and 1:30
656   am, respectively.

657   This study has displayed a comprehensive analysis of OT occurrences over near the globe
658   for the first time using MODIS data. As MODIS has a fine spatial resolution (1 km) and provides

659 about two-decade stable climate records, results in this study are an important complement to the
660 current OT climatology in literature derived from GPM, GOES and AMSU-B (Bedka et al.,
661 2018; Hong et al., 2008; Liu et al., 2020). This study also lays a foundation to understand near
662 global climatological distributions of hazardous thunderstorms, leading to valuable insights into
663 intense updraft size distributions in deep convection over the globe.

664

Data availability

666 CloudSat data including 2B-GEOPROF, 2B-CLDLASS-LIDAR and ECMWF-AUX, were
667 downloaded from https://www.cloudsat.cira.colostate.edu/.

668 GPM radar data is available at https://disc.gsfc.nasa.gov/datasets/GPM_2ADPR_07/summary.

669 MODIS data is available at https://ladsweb.modaps.eosdis.nasa.gov/.

670 MERRA-2 data can be downloaded at
671 https://goldsmr4.gesdisc.eosdis.nasa.gov/data/MERRA2/M2I1NXASM.5.12.4/.

672 The dataset used for training and cross-validating Logistic Regression is available in
673 Supplementary 2.

674 The dataset used for manually validating Logistic Regression is available in Supplementary 3.

675

Author contribution

677 YH, JT, SN and LDL conceived this study. YH performed the analysis, collected data, and wrote
678 the manuscript. SN collected data, helped with data analysis and edited the manuscript. JT
679 helped with interpretation of results and edited the manuscript. LD joined result discussions and
680 edited the manuscript.

Competing interests

682 The authors declare that they have no conflict of interest.

Acknowledgements

684 This work was mainly supported by the NASA award 80NSSC20K0902. The authors would like
685 to acknowledge Dr. Guangyu Zhao for his help in downloading the Terra MODIS data. We
686 thank the CloudSat Data Processing Center for providing CloudSat products, including 2B-
687 GEOPROF, 2B-CLDCLASS-LIDAR and ECMWF-AUX. We thank the Level-1 and
688 Atmosphere Archive & Distribution System (LAADS) Distributed Active Archive Center
689 (DAAC) for offering MODIS data (LAADS DAAC, 2022). We also acknowledge the NASA's
690 Goddard Earth Sciences Data and Information Services Center (GES DISC) for archiving
691 MERRA-2 data and GPM data (Iguchi and Meneghini 2021).

692

References

694 Ackerman, S. A.: Global satellite observations of negative brightness temperature differences

695 between 11 and 6.7 μm, J. Atmos. Sci., 53(19), 2803–2812, doi:10.1175/1520-
696 0469(1996)053<2803:GSOONB>2.0.CO;2, 1996.

697 Adams, D. K. and Comrie, A. C.: The North American Monsoon, Bull. Am. Meteorol. Soc.,
698 78(10), 2197–2213, doi:10.1175/1520-0477(1997)078<2197:TNAM>2.0.CO;2, 1997.

699 Alcala, C. M. and Dessler, A. E.: Observations of deep convection in the tropics using the
700 Tropical Rainfall Measuring Mission (TRMM) precipitation radar, J. Geophys. Res. Atmos.,
701 107(24), doi:10.1029/2002JD002457, 2002.

702 Astin, I., Di Girolamo, L. and Van De Poll, H. M.: Bayesian confidence intervals for true
703 fractional coverage from finite transect measurements: Implications for cloud studies from space,
704 J. Geophys. Res. Atmos., 106(D15), 17303–17310, doi:10.1029/2001JD900168, 2001.

705 Barnes, W. L., Pagano, T. S. and Salomonson, V. V.: Prelaunch characteristics of the moderate
706 resolution, IEEE Trans. Geosci. Remote Sens., 36, 1088–1100, 1998.

707 Bedka, K., Brunner, J., Dworak, R., Feltz, W., Otkin, J. and Greenwald, T.: Objective satellite-
708 based detection of overshooting tops using infrared window channel brightness temperature
709 gradients, J. Appl. Meteorol. Climatol., 49(2), 181–202, doi:10.1175/2009JAMC2286.1, 2010.

710 Bedka, K. M.: Overshooting cloud top detections using MSG SEVIRI Infrared brightness
711 temperatures and their relationship to severe weather over Europe, Atmos. Res., 99(2), 175–189,
712 doi:10.1016/j.atmosres.2010.10.001, 2011.

713 Bedka, K. M. and Khlopenkov, K.: A probabilistic multispectral pattern recognition method for
714 detection of overshooting cloud tops using passive satellite imager observations, J. Appl.
715 Meteorol. Climatol., 55(9), 1983–2005, doi:10.1175/JAMC-D-15-0249.1, 2016.

716 Bedka, K. M., Allen, J. T., Punge, H. J., Kunz, M. and Simanovic, D.: A long-term overshooting
717 convective cloud-top detection database over Australia derived from MTSAT Japanese
718 Advanced Meteorological Imager Observations, J. Appl. Meteorol. Climatol., 57(4), 937–951,
719 doi:10.1175/JAMC-D-17-0056.1, 2018.

720 Bosilovich, M. G., Lucchesi, R. and Suarez, M.: MERRA-2: File Specification, Earth, 9(9), 73
721 [online] Available from: http://gmao.gsfc.nasa.gov/pubs/office_notes., 2016.

722 Chung, E. S., Sohn, B. J., Schmetz, J. and Koening, M.: Diurnal variation of upper tropospheric
723 humidity and its relations to convective activities over tropical Africa, Atmos. Chem. Phys.,
724 2489–2502, doi:www.atmos-chem-phys.net/7/2489/2007/, 2007.

725 Chung, E. S., Sohn, B. J. and Schmetz, J.: CloudSat shedding new light on high-reaching tropical
726 deep convection observed with Meteosat, Geophys. Res. Lett., 35(2), 1–5,
727 doi:10.1029/2007GL032516, 2008.

728 Dworak, R., Bedka, K., Brunner, J. and Feltz, W.: Comparison between GOES-12 overshooting-
729 top detections, WSR-88D radar reflectivity, and severe storm reports, Weather Forecast., 27(3),
730 684–699, doi:10.1175/WAF-D-11-00070.1, 2012.

731 Funk, C., Verdin, A., Michaelsen, J., Peterson, P., Pedreros, D. and Husak, G.: A global satellite-
732 assisted precipitation climatology, Earth Syst. Sci. Data, 7(2), 275–287, doi:10.5194/essd-7-275-
733 2015, 2015.

734 Geerts, B., Giangrande, S. E., McFarquhar, G. M., Xue, L., Abel, S. J., Comstock, J. M.,
735 Crewell, S., DeMott, P. J., Ebell, K., Field, P., Hill, T. C. J., Hunzinger, A., Jensen, M. P.,
736 Johnson, K. L., Juliano, T. W., Kollias, P., Kosovic, B., Lackner, C., Luke, E., Lüpkes, C.,
737 Matthews, A. A., Neggers, R., Ovchinnikov, M., Powers, H., Shupe, M. D., Spengler, T.,
738 Swanson, B. E., Tjernström, M., Theisen, A. K., Wales, N. A., Wang, Y., Wendisch, M. and Wu,
739 P.: The COMBLE Campaign: A Study of Marine Boundary Layer Clouds in Arctic Cold-Air
740 Outbreaks, Bull. Am. Meteorol. Soc., 103(5), E1371–E1389, doi:10.1175/bams-d-21-0044.1,
741 2022.

742 Gettelman, A., Salby, M. L. and Sassi, F.: Distribution and influence of convection in the
743 tropical tropopause region, J. Geophys. Res. Atmos., 107(9–10), doi:10.1029/2001jd001048,
744 2002.

745 Gettelman, A., Forster, P. M. de F., Fujiwara, M., Fu, Q., Vo¨mel, H., Gohar, L. K., Johanson,
746 C. and Ammerman, M.: Radiation balance of the tropical tropopause layer, J. Geophys. Res.,
747 109(D7), D07103, doi:10.1029/2003JD004190, 2004.

748 Griffin, S. M.: Climatology of tropical overshooting tops in North Atlantic tropical cyclones, J.
749 Appl. Meteorol. Climatol., 56(6), 1783–1796, doi:10.1175/JAMC-D-16-0413.1, 2017.

750 Griffin, S. M., Bedka, K. M. and Velden, C. S.: A method for calculating the height of
751 overshooting convective cloud tops using satellite-based IR imager and CloudSat cloud profiling
752 radar observations, J. Appl. Meteorol. Climatol., 55(2), 479–491, doi:10.1175/JAMC-D-15-
753 0170.1, 2016.

754 Grise, K. M., Thompson, D. W. J. and Birner, T.: A global survey of static stability in the
755 stratosphere and upper troposphere, J. Clim., 23, 2275–2292, doi:10.1175/2009JCLI3369.1,
756 2010.

757 Groenemeijer, P., Púcik, T., Holzer, A. M., Antonescu, B., Riemann-Campe, K., Schultz, D. M.,
758 Kühne, T., Feuerstein, B., Brooks, H. E., Doswell, C. A., Koppert, H. J. and Sausen, R.: Severe
759 convective storms in Europe: Ten years of research and education at the European Severe Storms
760 Laboratory, Bull. Am. Meteorol. Soc., 98(12), 2641–2651, doi:10.1175/BAMS-D-16-0067.1,
761 2017.

762 Heymsfield, G. M., Tian, L., Heymsfield, A. J., Li, L. and Guimond, S.: Characteristics of deep
763 tropical and subtropical convection from nadir-viewing high-altitude airborne doppler radar, J.
764 Atmos. Sci., 67(2), 285–308, doi:10.1175/2009JAS3132.1, 2010.

765 Hong, G., Heygster, G., Miao, J. and Kunzi, K.: Detection of tropical deep convective clouds
766 from AMSU-B water vapor channels measurements, J. Geophys. Res. D Atmos., 110(5), 1–15,
767 doi:10.1029/2004JD004949, 2005.

768 Hong, G., Heygster, G., Notholt, J. and Buehler, S. A.: Interannual to diurnal variations in
769 tropical and subtropical deep convective clouds and convective overshooting from seven years of
770 AMSU-B measurements, J. Clim., 21(17), 4168–4189, doi:10.1175/2008JCLI1911.1, 2008.

771 Hong, Y. and Di Girolamo, L.: Cloud Phase Characteristics Over Southeast Asia from A-Train
772 Satellite Observations, Atmos. Chem. Phys., (20), 8267–8291, doi:https://doi.org/10.5194/acp-
773 20-8267-2020, 2020.

774 Hou, A. Y., Kakar, R. K., Neeck, S., Azarbarzin, A. A., Kummerow, C. D., Kojima, M., Oki, R.,
775 Nakamura, K. and Iguchi, T.: The global precipitation measurement mission, Bull. Am.
776 Meteorol. Soc., 95(5), 701–722, doi:10.1175/BAMS-D-13-00164.1, 2014.

777 Hourngir, D., Panegrossi, G., Casella, D., Sanò, P., D'adderio, L. P. and Liu, C.: A 4-year
778 climatological analysis based on gpm observations of deep convective events in the
779 mediterranean region, Remote Sens., 13(9), 1–21, doi:10.3390/rs13091685, 2021.

780 Janiga, M. A. and Thorncroft, C. D.: Convection over tropical Africa and the East Atlantic
781 during the West African monsoon: Regional and diurnal variability, J. Clim., 27(11), 4189–4208,
782 doi:10.1175/JCLI-D-13-00449.1, 2014.

783 Jeyaratnam, J., Luo, Z. J., Giangrande, S. E., Wang, D. and Masunaga, H.: A Satellite-Based
784 Estimate of Convective Vertical Velocity and Convective Mass Flux: Global Survey and
785 Comparison With Radar Wind Profiler Observations, Geophys. Res. Lett., 48(1), 1–11,
786 doi:10.1029/2020GL090675, 2021.

787 Johnson, R. H.: Diurnal cycle of monsoon convection, in The global monsoon system: Research
788 and forecast, pp. 257–276, Singapore: World Scientific., 2011.

789 Khlopenkov, K. V., Bedka, K. M., Cooney, J. W. and Itterly, K.: Recent Advances in Detection
790 of Overshooting Cloud Tops From Longwave Infrared Satellite Imagery, J. Geophys. Res.
791 Atmos., 126(14), 1–25, doi:10.1029/2020jd034359, 2021.

792 King, M. D., Kaufman, Y. J., Menzel, W. P. and Tanré, D.: Remote sensing of cloud, aerosol,
793 and water vapor properties from the Moderate Resolution Imaging Spectrometer (MODIS), IEEE
794 Trans. Geosci. Remote Sens., 30, 2–27, doi:10.1109/36.124212, 1992.

795 Li, H., Wei, X., Min, M., Li, B., Nong, Z. and Chen, L.: A Dataset of Overshooting Cloud Top
796 from 12-Year CloudSat/CALIOP Joint Observations, Remote Sens., 14(10), 2417,
797 doi:10.3390/rs14102417, 2022.

798 Liu, C. and Zipser, E. J.: Global distribution of convection penetrating the tropical tropopause, J.
799 Geophys. Res. Atmos., 110(23), 1–12, doi:10.1029/2005JD006063, 2005.

800 Liu, N. and Liu, C.: Global distribution of deep convection reaching tropopause in 1 year GPM
801 observations, NJournal Geophys. Res. Atmosperes, 121, 3924–3842, doi:10.1002/
802 2015JD024430, 2016.

803 Liu, N., Liu, C. and Hayden, L.: Climatology and Detection of Overshooting Convection From
804 4 Years of GPM Precipitation Radar and Passive Microwave Observations, J. Geophys. Res.
805 Atmos., 125(7), 1–14, doi:10.1029/2019JD032003, 2020.

806 Marchand, R., Mace, G. G., Ackerman, T. and Stephens, G.: Hydrometeor detection using
807 Cloudsat - An earth-orbiting 94-GHz cloud radar, J. Atmos. Ocean. Technol., 25(4), 519–533,
808 doi:10.1175/2007JTECHA1006.1, 2008.

809 Marion, G. R., Trapp, R. J. and Nesbitt, S. W.: Using overshooting top area to discriminate
810 potential for large, intense tornadoes, Geophys. Res. Lett., 46(21), 12520–12526,
811 doi:10.1029/2019GL084099, 2019.

812 Monette, S. A., Velden, C. S., Griffin, K. S. and Rozoff, C. M.: Examining trends in satellite-

813 detected tropical overshooting tops as a potential predictor of tropical cyclone rapid
814 intensification, J. Appl. Meteorol. Climatol., 51(11), 1917–1930, doi:10.1175/JAMC-D-11-
815 0230.1, 2012.

816 Murphy, A. M., Rauber, R. M., McFarquhar, G. M., Finlon, J. A., Plummer, D. M., Rosenow, A.
817 A. and Jewett, B. F.: A microphysical analysis of elevated convection in the comma head region
818 of continental winter cyclones, J. Atmos. Sci., 74(1), 69–91, doi:10.1175/JAS-D-16-0204.1,
819 2017.

820 Nesbitt, S. W. and Zipser, E. J.: The diurnal cycle of rainfall and convective intensity according
821 to three years of TRMM measurements, J. Clim., 16, 1456–1475, doi:10.1175/1520-0442-
822 16.10.1456, 2003.

823 Papritz, L., Rouges, E., Aemisegger, F. and Wernli, H.: On the Thermodynamic Preconditioning
824 of Arctic Air Masses and the Role of Tropopause Polar Vortices for Cold Air Outbreaks From
825 Fram Strait, J. Geophys. Res. Atmos., 124(21), 11033–11050, doi:10.1029/2019JD030570, 2019.

826 Partain, P.: Cloudsat ECMWF-AUX auxiliary data process description and interface control
827 document, Coop. Inst. Res. Atmos. Color. State Univ. [online] Available from:
828 http://129.82.109.192/ICD/ECMWF-AUX/ECMWF-AUX_PDICD_3.0.pdf, 2007.

829 Platnick, S., King, M. D., Ackerman, S. A., Menzel, W. P., Baum, B. A., Riédi, J. C. and Frey,
830 R. A.: The MODIS cloud products : Algorithms and examples from Terra, IEEE Trans. Geosci.
831 Remote Sens., 41, 459–473, doi:10.1109/TGRS.2002.808301, 2003.

832 Proud, S. R.: Analysis of overshooting top detections by Meteosat Second Generation: A 5-year
833 dataset, Q. J. R. Meteorol. Soc., 141(688), 909–915, doi:10.1002/qj.2410, 2015.

834 Rauber, R. M., Wegman, J., Plummer, D. M., Rosenow, A. A., Peterson, M., McFarquhar, G.
835 M., Jewett, B. F., Leon, D., Market, P. S., Knupp, K. R., Keeler, J. M. and Battaglia, S. M.:
836 Stability and charging characteristics of the comma head region of continental winter cyclones, J.
837 Atmos. Sci., 71(5), 1559–1582, doi:10.1175/JAS-D-13-0253.1, 2014.

838 Rauber, R. M., Plummer, D. M., Macomber, M. K., Rosenow, A. A., McFarquhar, G. M., Jewett,
839 B. F., Leon, D., Owens, N. and Keeler, J. M.: The role of cloud-top generating cells and
840 boundary layer circulations in the finescale radar structure of a winter cyclone over the great
841 lakes, Mon. Weather Rev., 143(6), 2291–2318, doi:10.1175/MWR-D-14-00350.1, 2015.

842 Rysman, J. F., Claud, C. and Delanoe, J.: Monitoring Deep Convection and Convective
843 Overshooting from 60° S to 60° N Using MHS: A Cloudsat/CALIPSO-Based Assessment, IEEE
844 Geosci. Remote Sens. Lett., 14(2), 159–163, doi:10.1109/LGRS.2016.2631725, 2017.

845 Schmetz, J., Tjemkes, S. A., Gube, M. and Van De Berg, L.: Monitoring deep convection and
846 convective overshooting with METEOSAT, Adv. Sp. Res., 19(3), 433–441, doi:10.1016/S0273-
847 1177(97)00051-3, 1997.

848 Setvák, M., Rabin, R. M. and Wang, P. K.: Contribution of the MODIS instrument to
849 observations of deep convective storms and stratospheric moisture detection in GOES and MSG
850 imagery, Atmos. Res., 83(2-4 SPEC. ISS.), 505–518, doi:10.1016/j.atmosres.2005.09.015, 2007.

851 Setvák, M., Bedka, K., Lindsey, D. T., Sokol, A., Charvát, Z., Šťástka, J. and Wang, P. K.: A-
852 Train observations of deep convective storm tops, Atmos. Res., 123, 229–248,

853   doi:10.1016/j.atmosres.2012.06.020, 2013.

854   Shikhov, A., Chernokulsky, A., Kalinin, N., Bykov, A. and Pischalnikova, E.: Climatology and
855   Formation Environments of Severe Convective Windstorms and Tornadoes in the Perm Region
856   (Russia) in 1984-2020, Atmosphere (Basel)., (12), 1407, doi:https://doi.org/
857   10.3390/atmos12111407, 2021.

858   Stephens, G. L., Vane, D. G., Boain, R. J., Mace, G. G., Sassen, K., Wang, Z., Illingworth, A. J.,
859   O'Connor, E. J., Rossow, W. B., Durden, S. L., Miller, S. D., Austin, R. T., Benedetti, A. and
860   Mitrescu, C.: The cloudsat mission and the A-Train: A new dimension of space-based
861   observations of clouds and precipitation, Bull. Am. Meteorol. Soc., 83, 1771–1790,
862   doi:10.1175/BAMS-83-12-1771, 2002.

863   Stephens, G. L., Vane, D. G., Tanelli, S., Im, E., Durden, S., Rokey, M., Reinke, D., Partain, P.,
864   Mace, G. G., Austin, R., L'Ecuyer, T., Haynes, J., Lebsock, M., Suzuki, K., Waliser, D., Wu, D.,
865   Kay, J., Gettelman, A., Wang, Z. and Marchand, R.: CloudSat mission: Performance and early
866   science after the first year of operation, J. Geophys. Res., 113, D00A18,
867   doi:10.1029/2008JD009982, 2008.

868   Stewart, R. E., Szeto, K. K., Reinking, R. F., Clough, S. A. and Ballard, S. P.: Midlatitude
869   cyclonic cloud systems and their features affecting large scales and climate, Rev. Geophys.,
870   36(2), 245–273, doi:10.1029/97RG03573, 1998.

871   Sun, L. X., Zhuge, X. Y. and Wang, Y.: A Contour-Based Algorithm for Automated Detection of
872   Overshooting Tops Using Satellite Infrared Imagery, IEEE Trans. Geosci. Remote Sens., 57(1),
873   497–508, doi:10.1109/TGRS.2018.2857486, 2019.

874   Tao, C. and Jiang, H.: Global distribution of hot towers in tropical cyclones based on 11-Yr
875   TRMM data, J. Clim., 26(4), 1371–1386, doi:10.1175/JCLI-D-12-00291.1, 2013.

876   Terpstra, A., Renfrew, I. A. and Sergeev, D. E.: Characteristics of cold-air outbreak events and
877   associated polar mesoscale cyclogenesis over the north Atlantic region, J. Clim., 34(11), 4567–
878   4584, doi:10.1175/JCLI-D-20-0595.1, 2021.

879   Tian, B., Soden, B. J. and Wu, X.: Diurnal cycle of convection, clouds, and water vapor in the
880   tropical upper troposphere: Satellites versus a general circulation model, J. Geophys. Res. D
881   Atmos., 109(10), 1–16, doi:10.1029/2003JD004117, 2004.

882   Tian, B., Held, I. M., Lau, N. C. and Soden, B. J.: Diurnal cycle of summertime deep convection
883   over North America: A satellite perspective, J. Geophys. Res. D Atmos., 110(8), 1–10,
884   doi:10.1029/2004JD005275, 2005.

885   Trapp, R. J., Marion, G. R. and Nesbitt, S. W.: The regulation of tornado intensity by updraft
886   width, J. Atmos. Sci., 74(12), 4199–4211, doi:10.1175/JAS-D-16-0331.1, 2017.

887   Vergados, P., Luo, Z. J., Emanuel, K. and Mannucci, A. J.: Observational tests of hurricane
888   intensity estimations using GPS radio occultations, J. Geophys. Res. Atmos., 119, 1936–1948,
889   doi:10.1002/2013JD020934, 2014.

890   Wang, C., Luo, Z. J. and Huang, X.: Parallax correction in collocating CloudSat and Moderate
891   Resolution Imaging Spectroradiometer (MODIS) observations: Method and application to
892   convection study, J. Geophys. Res. Atmos., 116(17), 1–9, doi:10.1029/2011JD016097, 2011.

893 Wang, Z., Vane, D. and Staphens, G.: Level 2 Combined Radar and Lidar Cloud Scenario
894 Classification Product Process Description and Interface Control document. [online] Available
895 from:
896 http://scholar.google.com/scholar?hl=en&btnG=Search&q=intitle:Level+2+Combined+Radar+a
897 nd+Lidar+Cloud+Scenario+Classification+Product+Process+Description+and+Interface+Contro
898 l+Document#1, 2012.

899 Wilcox, L. J., Hoskins, B. J. and Shine, K. P.: A global blended tropopause based on ERA data.
900 Part I: Climatology, Q. J. R. Meteorol. Soc., 138(664), 561–575, doi:10.1002/qj.951, 2012.

901 Winker, D. M., Pelon, J. R. and McCormick, M. P.: The CALIPSO mission: Spaceborne lidar for
902 observation of aerosols and clouds, Lidar Remote Sens. Ind. Environ. Monit. III, 4893, 1–11,
903 doi:10.1117/12.466539, 2003.

904 Xiong, X., Sun, J., Wu, A., Chiang, K.-F., Esposito, J. and Barnes, W.: Terra and Aqua MODIS
905 calibration algorithms and uncertainty analysis, Sensors, Syst. Next-Generation Satell. IX,
906 5978(November 2015), 59780V, doi:10.1117/12.627631, 2005.

907 Xiong, X., Angal, A., Barnes, W. L., Chen, H., Chiang, V., Geng, X., Li, Y., Twedt, K., Wang,
908 Z., Wilson, T. and Wu, A.: Updates of Moderate Resolution Imaging Spectroradiometer on-orbit
909 calibration uncertainty assessments, J. Appl. Remote Sens., 12(03), 1,
910 doi:10.1117/1.jrs.12.034001, 2018.

911 Yuter, S. E. and Houze, R. A.: Three-dimensional kinematic and microphysical evolution of
912 Florida cumulonimbus. Part II: Frequency distributions of vertical velocity, reflectivity, and
913 differential reflectivity, Mon. Weather Rev., 123, doi:https://doi.org/10.1175/1520-
914 0493(1995)123<1941:TDKAME>2.0.CO;2, 1995.

915 Zhuge, X. Y., Ming, J. and Wang, Y.: Reassessing the use of inner-core hot towers to predict
916 tropical cyclone rapid intensification, Weather Forecast., 30(5), 1265–1279, doi:10.1175/WAF-
917 D-15-0024.1, 2015.

918 Zipser, E. J., Cecil, D. J., Liu, C., Nesbitt, S. W. and Yorty, D. P.: Where are the most intense
919 thunderstorms on Earth?, Bull. Am. Meteorol. Soc., 87(8), 1057–1071, doi:10.1175/BAMS-87-
920 8-1057, 2006.

921